*Tellus* (1988), *40A*, 358–374

# Modes of variability in a low-order two-level model

By ENDA O'BRIEN and LEE E. BRANSCOME, *University of Miami, Rosenstiel School of Marine and Atmospheric Science, Miami, Florida 33149, USA*

(Manuscript received 7 July 1987; in final form 5 February 1988)

ABSTRACT

A low-order, two-level model in a beta-plane channel is integrated over long periods of time to study low-frequency mid-latitude variability. The model allows for nonlinear wave-wave and wave-mean flow interactions as well as zonally asymmetric forcing by topography. Time scales for the forcing and damping terms are varied, and, for closer analysis, values are chosen according to best estimates for the earth. A damping parameter, compensating for unresolved scales, is introduced at the shortest resolved length scale to prevent a spurious build-up of energy at this scale. Flow patterns are produced which are highly variable and seemingly chaotic, not suggestive of trajectories around multiple equilibria or distinct strong attractors in phase space. Analysis of the model integrations reveals the existence of low-frequency variability in the form of slowly-propagating Rossby waves, wave amplitude modulation and persistent anomalies in the height fields, which satisfy magnitude and duration criteria. Such anomalies have an equivalent barotropic structure and tend to occur in certain preferred regions and have preferred signs for larger threshold criteria. Similar anomalies were found in integrations without topography, but were evenly distributed geographically, fewer in number and not as long-lived.

## 1. Introduction

For many years, there has been particular interest in the phenomenon of atmospheric blocking. This interest has recently broadened to encompass persistent anomalies in general. A "persistent anomaly" is defined as a deviation from the time mean of a minimum specified magnitude for a minimum specified time. In an observational study, Dole and Gordon (1983) found many anomalies in 500 mb height fields which exceeded substantial magnitude thresholds for periods of a week or more. Positive events often corresponded to classical blocking configurations.

Persistent anomalies and blocking events, in particular, have also been found in numerical models. Blackmon et al. (1986) found a good correspondence between the statistics of blocks in a 20-winter data set of 500 mb height analyses and in a 1200 day run of a general circulation model (GCM).

While blocks and persistent anomalies have been observed in the atmosphere and in the results of GCMs, similar events have not been well documented in less sophisticated models. Egger (1978) produced blocks in a mid-latitude $\beta$-plane model which allowed for interactions between orographically forced waves and slow-moving transient planetary waves. No dissipation or thermal forcing was included, however, and the orographic forcing was a straightforward eddy momentum forcing rather than a flow guide to induce vertical motion at the lower boundary. The model was, therefore, energetically open and could not be integrated over long periods.

Very severely truncated models, which include some kind of asymmetric forcing such as uneven bottom topography, have been found to possess multiple equilibrium solutions (e.g., Charney and deVore, 1979; Charney and Straus, 1980; Källén, 1981). Typically, one equilibrium state consists of a strong zonal flow and a weak wave, while another has weak zonal flow with a large-amplitude wave just out of resonance with the underlying topography. This latter configuration

is suggestive of blocking situations in the atmosphere and so it was proposed that blocks might be the atmospheric manifestation of certain stable equilibria.

This idea was tested further by Reinhold and Pierrehumbert (1982), henceforth referred to as RP, who relaxed the truncation of the Charney and Straus model to include one extra wave in the zonal direction. This transient synoptic-scale wave allowed for wave-wave as well as wave-mean flow interactions and destabilized all equilibria of the Charney and Straus model. The most important result of their experiments was that, for a wide parameter range, the model was observed to settle into one of two distinct flow configurations or "weather regimes" for extended periods of time, typically between 100 to 1000 days. In fact, the model flow fell into one regime or the other over 97% of the time. Each regime corresponded to the trajectory of the large-scale wave being confined to a narrow region of phase space, and corresponded to opposite phases of a quasi-stationary long wave. Still, the transition from multiple equilibria to multiple regimes, effected by the extra short-scale zonal wave, preserved the notion that multiple preferred states exist for the atmosphere.

It was proposed in RP that the regimes were maintained by the time-averaged effects of the high frequency transients, while the instantaneous effects were responsible for transitions between the regimes. However, Mukougawa (1986) found that the properties of the transients are largely independent of the basic state and concluded that topographic instability could better explain the regime transitions.

Cehelsky and Tung (1987, henceforth referred to as CT) expanded the RP model to include up to 10 wave modes in the zonal and meridional directions, and found that the attractor basin for the large-scale wave converged to a single small region in phase space, i.e., that the two regimes of RP were replaced by a single regime as the resolution was increased. This finding supports the claim by Tung and Rosenthal (1985) that results based on truncated, low-order models change drastically when full nonlinearity is retained (cf. Shukla and Mo, 1983, and Legras and Ghil, 1985), although this was not the case in Källén's (1982) high resolution barotropic model.

The converged model behavior at high resolutions obtained by CT still does not correspond to the behavior of the large-scale flow in the atmosphere. A possible explanation for this is that very short damping time scales were used by them (and by RP). Such short time scales are unrealistic, however, and are likely to distort the model climate by making the damping time scales as short as the $e$-folding time for the growth of an unstable baroclinic wave, thus preventing these waves from experiencing their normal life-cycle.

In this study, the parameters involving forcing and damping times were varied from the values given in RP to see how the model behavior changed in response. We found that the regime-type behavior of the RP model vanished when the forcing and damping time scales were lengthened. Either a single-wave equilibrium or a very chaotic flow appeared, depending on the ratio of the forcing and dissipation parameters. For further analysis, parameters were fixed at values more representative of the atmosphere. An extra parameter was also included at this stage to compensate for the dissipative or cascade effects of smaller length scales not explicitly resolved. This modification led to a more even distribution of energy among the resolved scales and a chaotic flow. The nature of the low-frequency variability and the existence of persistent anomalies only emerged from a closer analysis.

## 2. Model outline

The model used in this study is almost identical in formulation to that of RP and CT and will only be summarized here. We consider a quasi-geostrophic, two-layer, beta-plane channel model between zonal walls. Let the subscripts U and L refer to the upper and lower layers, respectively. Then let $\Psi = (\Psi_U + \Psi_L)/2$ be the vertical mean or barotropic streamfunction, $\tau = (\Psi_U - \Psi_L)/2$ the shear or baroclinic streamfunction, $\theta = (\theta_U + \theta_L)/2$ the mean potential temperature and $\sigma = (\theta_U - \theta_L)$ the static stability, which is assumed constant. The governing equations are then the barotropic and baroclinic vorticity equations and the thermodynamic equation, respectively:

$$\partial \nabla^2\Psi/\partial t + J(\Psi,\nabla^2\Psi) + J(\tau,\nabla^2\tau) + \beta\partial\Psi/\partial x = 0.5J(\tau - \Psi, fh_0/H) + 0.5k\nabla^2(\tau - \Psi), \quad (1)$$

$$\partial\nabla^2\tau/\partial t + J(\Psi,\nabla^2\tau) + J(\tau,\nabla^2\Psi) + \beta\partial\tau/\partial x = -fw/H + 0.5J(\Psi - \tau, fh_0/H) + 0.5k\nabla^2(\Psi - \tau) - 2k'\nabla^2\tau \quad (2)$$

$$\partial\theta/\partial t + J(\Psi,\theta) + \sigma w/H = \lambda(\theta^* - \theta). \quad (3)$$

The notation is similar to that of RP and CT and is mostly standard. Here $w$ is the vertical motion at the interface; $k$ and $k'$ the Ekman damping coefficients at the surface and between the layers, respectively; $f$ and $\beta$ the Coriolis parameter and its derivative at the center of the channel, $H$ the mean thickness of each layer, $h_0$ the topographic height, $\lambda$ the Newtonian cooling coefficient, $\theta^*$ a prescribed potential temperature field in radiative equilibrium and $J$ the horizontal Jacobian operator. The system of equations is closed by the thermal wind relation

$$\nabla^2\tau = A\nabla^2\theta \quad (4)$$

where $A$ is a constant factor as in RP and CT.

The equations are non-dimensionalized by choosing a suitable scaling. The horizontal coordinates are scaled by the length scale $L$ such that $x = Lx'$ and $y = Ly'$. We assume the channel is periodic in $x'$ over the scale $2\pi/n$ with no flow through, or net drag on, the walls at $y' = 0$ and $y' = \pi$. The parameter $n$ is dimensionless zonal wavenumber. All dependent and specified forcing variables are expanded in orthonormal eigenfunctions, $F_i(x',y')$, of the dimensionless Laplace operator with $\nabla^2 F_i = -a_i^2 F_i$. Thus, we have

$$\begin{aligned} \Psi &= L^2 f\left(\sum \Psi_i F_i\right) & w &= -fH\left(\sum \omega_i F_i\right) \\ \tau &= L^2 f\left(\sum \tau_i F_i\right) & h_0 &= H\left(\sum h_i F_i\right) \\ \theta &= AL^2 f\left(\sum \theta_i F_i\right) & \theta^* &= AL^2 f\left(\sum \theta^*_i F_i\right) \end{aligned} \quad (5)$$

where the subscripted dimensionless variables are functions of time, which is scaled by $f^{-1}$. Static stability $\sigma$ is scaled by $AL^2\sigma_0 f$, and $\lambda$, $k$ and $k'$ are all scaled by $f$. Note that $\tau_i = \theta_i$ from (4) and (5).

Substituting the above expressions into the original eqs. (1)-(3) yields the dimensionless equations

$$d\Psi_i/dt = a_i^{-2}\sum_j \sum_{j>k} c_{ijk}[(a_j^2 - a_k^2)(\Psi_j\Psi_k + \theta_j\theta_k) + 0.5h_j(\theta_k - \Psi_k) + 0.5h_k(\Psi_j - \theta_j)] + \beta' a_i^{-2}\sum_j b_{ij}\Psi_j - 0.5k(\Psi_i - \theta_i) \quad (6)$$

$$d\theta i/dt = a_i^{-2}\sum_j \sum_{j>k} c_{ijk}[(a_j^2 - a_k^2)(\Psi_j\theta_k + \theta_j\Psi_k) - 0.5h_j(\theta_k - \Psi_k)] - 0.5h_k(\Psi_j - \theta_j)] + \beta' a_i^{-2}\sum_j b_{ij}\theta_j - a_i^{-2}\omega_i + 0.5k\Psi_i - (0.5k + 2k')\theta_i \quad (7)$$

$$d\theta_i/dt = \sum_j \sum_{j>k} c_{ijk}(\Psi_k\theta_j - \theta_k\Psi_j) + \sigma_0\omega_i + \lambda(\theta_i^* - \theta_i) \quad (8)$$

where $c_{ijk} = (n/2\pi^2)\iint F_i J'(F_j,F_k)dx'dy'$ are the interaction coefficients, $J'$ is the dimensionless Jacobian, $b_{ij} = (n/2\pi^2)\iint F_i(\partial F_j/\partial x')dx'dy'$ and $\beta' = \beta L/f$. The eigenvalues $a_i^{-2}$ can be found by operating on each $F_i$ with the Laplacian.

Truncating the expansion at two waves in $x$ and two waves in $y$ gives the fewest possible number of components that provides a planetary scale, a short synoptic scale and non-zero wave-wave interaction coefficients. This means that ten eigenfunctions $F_i$ are kept as follows:

| *Mode 01* | *Mode 02* |
|---|---|
| $F_1 = \sqrt{2}\cos y'$ | $F_2 = \sqrt{2}\cos 2y'$ |
| *Mode 11* | *Mode 12* |
| $F_2 = 2\sin y'\cos nx'$ | $F_5 = 2\sin 2y'\cos nx'$ |
| $F_3 = 2\sin y'\sin nx'$ | $F_6 = 2\sin 2y'\sin nx'$ |
| *Mode 21* | *Mode 22* |
| $F_7 = 2\sin y'\cos 2nx'$ | $F_9 = 2\sin 2y'\cos 2nx'$ |
| $F_8 = 2\sin y'\sin 2nx'$ | $F_{10} = 2\sin 2y'\sin 2nx'$ |

Here the zonal wavenumber $n$ may be chosen freely. It is related to the planetary zonal wavenumber, $m$, by $m = (na\cos\phi_0)/L$ where $a$ is the earth's radius and $\phi_0$ is the central latitude of the channel.

The $\omega_i$ components may be eliminated from (7) and (8), leaving a single equation for each $\theta_i$ component. The spectral form of the model then consists of 20 ordinary differential equations for the amplitude coefficients of the 10 eigenfunctions of the streamfunction, $\Psi$, and the potential temperature, $\theta$. Only the amplitude of the $F_2$ topography component, $h_2$, and the $F_1$ heating component, $\theta^*_1$, are taken different from zero. This system was integrated using the $N$-cycle scheme of Lorenz (1971) with $N = 4$ and a timestep of 1.5 h. All model runs were continued out for 1100 model days, but only the last 1000 days were used for analytic or statistical purposes.

## 3. Model scaling and response to variation of parameters

Two ideally complementary, but sometimes conflicting, principles are involved in the assignment of model parameters. The first is that each physical parameter should be set to a realistic value for the atmosphere. The second is that the model should realistically simulate the atmospheric circulation. As a possible consequence of an initial algebraic error (cf. Corrigendum to their paper, 1985), RP found that it was not possible to simultaneously satisfy both these restrictions. Therefore, they opted to adjust some of the parameter values in order to achieve as realistic a model circulation as possible. This involved shortening the $e$-folding radiative and dissipative time scales to the point where they were about the same as the growth rate for an unstable baroclinic wave. This, in turn, led to further distortion of the model climate as these unstable waves were prevented from experiencing their normal life-cycle, and gave rise to the exaggeration of weather regime persistence.

Apart from the forcing and dissipation time scales, we assigned the same values to the other parameters as in the RP "demonstration case", since these correspond to an earth-like situation. Thus, the channel width $\pi L$ was set to 5000 km and $A$ to $1.18 \times 10^{-6}$ m$^{-2}$ s K. Other parameters were fixed as follows:

$$\beta' = 0.2, \quad \theta^*_1 = 0.1,$$
$$\sigma_0 = 0.1, \quad n = 1.3, \quad h_2 = 0.2$$

Dimensionally these choices set the central latitude of the channel at 51°, a meridional temperature difference of 72°C across the channel at radiative equilibrium, a squared Brunt-Väisälä frequency of $10^{-4}$s$^{-2}$, a zonal wavelength of 7700 km (corresponding to a planetary wavenumber 3) for the long wave in the model and a dimensional mountain height of 3.2 km from valley to peak.

In the "demonstration case" parameter settings of RP, the Newtonian cooling coefficient $\lambda$ and the Ekman damping coefficients k and k′ are assigned the dimensional values $(\lambda^{-1}, k^{-1}, k'^{-1})$ = (2.5, 1.125, 11.25) days, respectively. These time scales are much shorter than generally accepted values for the atmosphere. Other modellers using similar Newtonian cooling parametrizations set the relaxation time at 10 days (Charney and Straus, 1980) or 15 days (Hendon, 1986). The frictional dissipation time scale due to the surface boundary layer was set at 5 days by Hendon (1986), 10 days by Charney and Straus (1980) and 12 days by Barnes (1986). The dissipation at the mid-level interface is peculiar to this model. However, it should only amount to a small fraction of the dissipation caused by the surface boundary layer.

The model was run for 1100 days with several different values of $k$, $k'$ and $\lambda$ to see how the gross features of the flow depended on these parameters. Each of the three was varied singly (with the other two at the RP values), as well as in a constant ratio to each other. As in RP, we used the phase of the large-scale mode 11 wave as a measure of regime tendency in the model. Their "ridge" regime had a strong ridge in the 500 mb height field about 90° west of the mountain peak and corresponded to $\Psi_2 > 0$ and $\Psi_3 < 0$. Their "trough" regime had a 500 mb trough 45° west of the mountain peak and had $\Psi_2 < 0$ and $\Psi_3 > 0$. In other words, for one regime the phase of mode 11 was in the second quadrant of $(\Psi_3, \Psi_2)$ phase space, and for the other regime it was in the fourth quadrant.

For each run, we counted the number of times the mode 11 phase entered each quadrant and measured the amount of time it spent in each quadrant as a percentage of the total time (i.e. the last 1000 of the 1100 days). When the circulation is dominated by stationary waves (or regimes), the mode 11 phase enters each "regime" quad-

rant relatively few times but spends a large percentage of total time there. When chaotic or propagation tendencies dominate, the mode 11 phase enters and leaves each quadrant more often and spends roughly equal amounts of time in each quadrant.

Some measurements obtained for these crude indices are shown in Fig. 1, which gives an indication of the nature of the flow as the surface friction time scale, $k^{-1}$, varies. As this time scale is increased from its RP value ($k^{-1}$ = 1.125 days) the model shows consistently less tendency towards regime-type behavior. For 1-day friction, the phase enters the second quadrant (the circles in Fig. 1) 23 times in 1000 days, and 192 times for 50-day friction. Corresponding numbers for entering the fourth quadrant (the triangles in Fig. 1) are 17 and 255, respectively. For 1-day friction, the phase is in the second quadrant 49% of the time (+ symbols) and in the fourth quadrant 39% of the time (× symbols). For 50-day friction, it spends 35% of the time in the second quadrant and 15% of the time in the fourth. To put these numbers in perspective, a steadily propagating wave with a period of 10 days would enter each quadrant 100 times in 1000 days and spend 25% of the time in each quadrant.

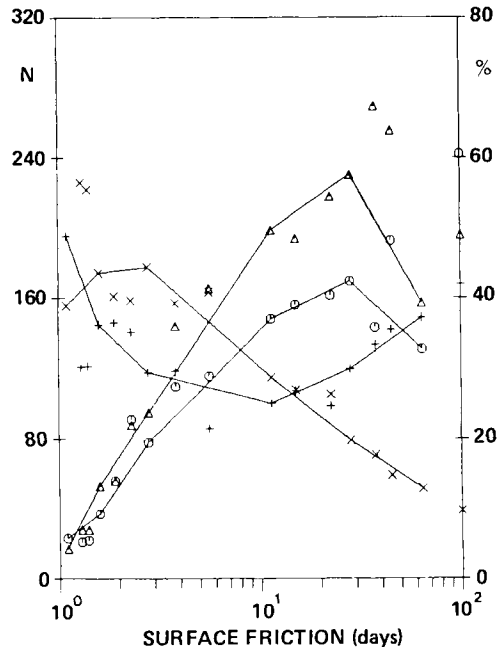


*Fig. 1.* Number of times, $N$, per 1000 days that phase of mode 11 wave entered second quadrant (circles) and fourth quadrant (triangles), as a function of dimensional $k^{-1}$. Ordinate for these curves is shown on left. % of total time mode 11 phase spent in second quadrant (+ symbols) and fourth quadrant (× symbols) is plotted with respect to scale on right. Lines are drawn through every third point to highlight underlying trends.

In Fig. 1 every third data point is joined by a straight line in order to highlight the trends as the friction time scale is lengthened. More objective means, including least-squares approximations to the scatter of points, were unhelpful for this purpose. The finite integration time probably leads to a certain spurious scatter in the experimental results. However, some of the large differences in phase behaviour for slightly different friction values may also be due to the phase falling randomly into different strong attractors. Nevertheless, gross trends are discernable, as shown by the connecting lines. For short frictional time scales, the two stationary waves of opposite phase are clearly dominant. As the time scale is lengthened, the phase of the mode 11 wave becomes more evenly distributed among all four quadrants, reflecting (in all these cases) an increasing chaos of the flow. For very weak friction (50-day time scales or longer), the number of times the phase enters each quadrant appears to approach a limiting value. This hypothesis was verified by a run with zero surface friction. On the other hand, the phase spends significantly less time in the fourth quadrant than in the second, opposite to the situation for most experiments with strong friction. As friction time scales are lengthened, the mode 11 amplitude also increases, and for time scales longer than 30 days or so the flow is probably just as unrealistic as it is for time scales of about one day.

As the radiative time scale, $\lambda^{-1}$, is gradually lengthened from its RP value of 2.5 days, regime-type behavior is initially enhanced. The phase of the mode 11 wave spends almost all the time in either the second or fourth quadrants and undergoes fewer transitions from one to the other. The amplitude of this wave also gets smaller. When $\lambda$ corresponds to about a 4-day time scale or longer, the mode 11 wave vanishes altogether after an initial period of growth, and the flow evolves into a single-wave equilibrium system with a constant mean flow and a constant-amplitude propagating mode 22 wave.

Mode 22 is not the *most* unstable wave in the linear sense. But, because of the truncation, it is the only wave which does not undergo wave-wave interactions. All other waves are linked via wave-wave interactions, and so when one is excited, the rest must be excited also. The most unstable wave according to linear analysis is mode 21, which has the lowest critical shear for instability. Other waves, which are linked to mode 21 by wave-wave interactions, are stable at this lowest critical shear and so serve merely to damp the mode 21 wave. Thus, the *effective* critical shear for mode 21 in the full nonlinear model is raised above the linear critical shear for the wave by itself. The critical shear for mode 22, however, is not affected by the presence of other waves in the full model, allowing this mode to reach large amplitudes.

Evidently, as $\lambda^{-1}$ is lengthened, the vertical shear is restored so slowly by the forcing that the damping effect of the wave-wave interactions becomes more efficient. At a certain value of $\lambda^{-1}$ they become so efficient that the effective critical shear for mode 21 is raised above the critical shear for mode 22, which then becomes the dominant and, effectively, most unstable wave. In the full model, baroclinic adjustment processes act to reduce the zonal mean shear, as represented by $\theta_1$, to the extent where only mode 22 is unstable. This wave then exists by itself, extracting enough energy from the mean flow to keep the shear at the neutral value and stable to perturbations in all the other waves.

Thus, a critical value of the Newtonian cooling time scale, $\lambda^{-1}$, seems to exist, above which the model flow settles into a single-wave (mode 22) equilibrium and below which all resolved waves remain excited. When all other parameters are as in RP, this critical value is between 4 and 4.5 days. Similarly, a critical value of the interface friction exists, for $k'^{-1}$ somewhere between 16 and 19 days. The model responds to changes in $k'$ almost exactly the same as for $\lambda$. But, this effect of reduced interface friction cannot be immediately explained in the same way as the effect of slower Newtonian cooling. Reduced interface friction should allow for greater baroclinicity in the model and, therefore, more instability. A possible explanation may be that the larger vertical shears in the wave components allow the waves to be more efficient in reducing the mean vertical shear, thus eventually stabilizing all the waves except mode 22. Reducing interface friction corresponds to *increasing* surface friction in the sense that they both allow stronger vertical shears.

In an attempt to compensate for the opposing effects of weaker surface friction on one hand, and longer radiative and interfacial friction times on the other, the model was run with $k$, $k'$ and $\lambda$ reduced together while kept in the same ratio as in RP. Again, the single-wave (mode 22) equilibrium appeared once these parameters were reduced to 0.7 times their RP values. Even at 70% of their RP values, these parameters remain unrealistically large.

When the model falls, or almost falls, into a single-wave equilibrium, it is because the radiative relaxation and dissipative time scales are so long that the most unstable wave can extract energy from the mean flow faster than it can be replenished by the thermal forcing. When the radiative and dissipative time scales are shortened to their RP values, the thermal forcing is strong enough to replenish the zonal mean energy faster than short wave instability can deplete it, and so zonal mean energy is available for long wave instability as well. This result is similar to that obtained by Yoden (1983).

It seems, therefore, that the appearance of regimes in the RP model is an artifact of the very short forcing and damping time scales. Moreover, making these time scales more realistic merely produces a circulation consisting of a steady mean flow with $\Psi_1 = \theta_1$ (i.e., no lower-layer mean flow) and a constant amplitude, eastward-propagating mode 22 wave.

## 4. Extra damping at the shortest scale

In pursuit of the ideal that earth-like parameter settings should lead to earth-like behavior, the parameters $\lambda^{-1}$, $k^{-1}$ and $k'^{-1}$ were fixed in this study at the more realistic values of 12.5, 11.25 and 45 days, respectively. The model was also run with a surface friction time scale of 5.625 days, although most of the results presented in this paper are for the weaker dissipation case. These values are all outside the range used in RP.

Using the parameter values as described above, including topography ($h_2 = 0.2$), the model

was integrated from the initial state of symmetric or "Hadley" equilibrium plus a small perturbation in all wave modes. The "Hadley" equilibrium is very close to radiative equilibrium and simply consists of a zonal mean vertically sheared flow with no flow in the lower layer. In terms of the model variables this equilibrium is

$$\Psi_1 = \theta_1 = \lambda\theta^*_1/(\lambda + 2k'\sigma_0),$$
$$\Psi_i = \theta_i = 0, \quad i = 2, \ldots 10.$$

This flow is linearly unstable to perturbations in any of the wave modes.

Part of the time series of three barotropic components from this integration are shown in Fig. 2. The most notable aspect of this figure is that the mode 22 component $\Psi_9$ is the most energetic. This component is part of a large-amplitude baroclinic wave propagating eastward in a more or less regular fashion with a period of just over 12 days. Both the long wave, $\Psi_2$, and mean flow, $\Psi_1$, components have smaller amplitudes, although most of the aperiodic and chaotic nature of the flow is evident at these

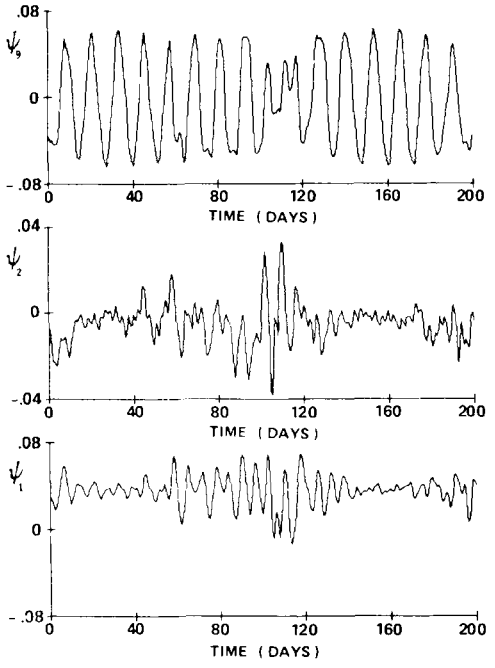


*Fig. 2.* Time series of barotropic streamfunction components $\Psi_9$, $\Psi_2$ and $\Psi_1$; $\lambda^{-1}$, $k^{-1}$ and $k'^{-1}$ are fixed at 12.5 days, 11.25 days and 45 days, respectively.

scales. In fact, over 66% of the time-mean kinetic energy in the entire system is concentrated in the shortest mode 22 wave, whereas the mode 11 wave only accounts for 3% of the total kinetic energy. This illustrates the fact that in the nonlinear sense, i.e., when the damping effect of wave-wave interactions are considered, the *linearly* most unstable mode 21 is rendered less unstable than mode 22, which is involved in wave-mean flow interactions only. Indeed, when the surface friction is doubled in strength (to $k^{-1} = 5.625$ days), the flow again falls into the single-wave equilibrium as described above.

This configuration is identical to a single wave ("S") equilibrium described by Cai and Mak (1987) and is stable to large perturbations in all wave modes. The properties of such an "S" equilibrium (a mean flow with one wave) have also been examined by Mak (1985). If the model were deliberately truncated to just one wave and a mean flow, as done by Mak, it would behave as the spectral analogue to Pedlosky's (1970) theory of weakly nonlinear baroclinic equilibration. Wave growth has the same dependence on a critical vertical shear below which the "Hadley" flow is stable. In both weakly nonlinear theory and this model, the wave-mean flow system with sufficiently strong frictional damping tends asymptotically to a state like a single-wave equilibrium. In an inviscid environment the system falls into a limit cycle, with energy continually exchanged between the mean flow and the wave like a particle oscillating in a potential well.

While it is of interest from the point of view of baroclinic equilibration, the single-wave equilibrium configuration is not a realistic atmospheric flow since it is so steady and other wave modes remain suppressed. We prefer a situation where the long planetary waves can exist and energy is continuously exchanged among the wave modes, as is the case in the atmosphere. Even in the run with weaker surface friction ($k^{-1} = 11.25$ days), the shortest scale dominates the flow and prevents the model from undergoing realistic variability.

One means of preventing a spurious build-up of energy at the short scale is to introduce an extra frictional damping at this scale only, while keeping the other dissipative parameters fixed at realistic values. This extra damping is analogous to that used by Salmon (1980) to remove the

baroclinic enstrophy which builds up at the shortest scale as a consequence of the finite truncation.

In the present model the finite truncation is such that the shortest scale cannot participate in the energy and enstrophy cascade process because it cannot engage in wave-wave interactions. Furthermore, this scale is unstable and can directly siphon energy from the mean flow without interacting with other waves. If mode 22 were stable, it would not dominate the flow, but simply die out. Shortening the forcing and damping time scales as in RP is effectively an attempt to stabilize this wave.

Alternatively, if more waves were included in the model, they would act as energy sinks for all the waves which can extract energy from the mean flow. Apart from a mode 13 wave, all waves shorter than mode 22 could only be excited by the cascade process of wave-wave interactions, as their wavenumber would be higher than the short-wave cutoff for baroclinic instability. Mode 22 would then be involved in wave-wave interactions with even shorter, stable waves, which would have a damping influence on mode 22, preventing it from dominating the flow as it does in the present model.

Extra damping of the mode 22 wave is introduced as a substitute for this cascade process. It serves to crudely, but explicitly, compensate for the severe spectral truncation and, as it turns out, the model then behaves in a more realistic way when all the other parameters are given realistic values. When a similar device was employed by CT, they found that their model converged to the single regime behavior at much lower resolutions than was otherwise the case. This extra term is added to the right hand side of the equations for $\Psi_9$, $\Psi_{10}$, $\theta_9$ and $\theta_{10}$ in (6) and (7) as follows:

$$d\Psi_i/dt = \ldots \text{(other terms)} \ldots - \alpha\Psi_i$$
$$(\sigma_0 + 1/(4n^2 + 4))d\theta_i/dt = \ldots \text{ (other terms) } \ldots - \alpha\sigma_0\theta_i \quad i = 9,10.$$

The extra damping is homogeneous and the coefficient $\alpha$ is the same in both layers. It does not have the form of Ekman damping which acts at a boundary or interface.

There is no clear physical basis for choosing a value for $\alpha$. Salmon (1980) chose $\alpha$ so that the energy spectrum looked smooth at high wavenumbers. In this study, the model (including topography) was run several times at different values of $\alpha^{-1}$ ranging from 1 day to 22 days. For the stronger surface friction case ($k^{-1} = 5.625$ days) the most notable result was that even the smallest value of $\alpha$ ($\alpha^{-1} = 22$ days) prevented the model from falling into a single wave equilibrium as happens for $\alpha = 0$, and allowed energy to be distributed among all wave modes and exchanged in an apparently irregular fashion as the integration proceeded.

In general, for both the weaker and stronger settings of surface dissipation, increasing the value of $\alpha$ caused an increase in the ratio of energy in long waves to energy in the short waves. Not surprisingly, as $\alpha$ was increased, energy in the short waves was reduced more than energy in the long waves was increased. The short wave time series also became more chaotic. Apart from these effects, varying the value of $\alpha$ *did not alter any other qualitative aspect of the flow*. For each model component the time series show the same kind of irregularities and quasi-periodicities independent of the value of $\alpha$, as long as it is greater than zero. Increasing $\alpha$ by a factor of four (from $\alpha^{-1} = 22$ days to 5.5 days) causes an 18% decrease in mean energy and an 8% decrease in the energy standard deviation. Increasing $\alpha$ by a factor of 10 (to $\alpha^{-1} = 2.2$ days) leads to similar reductions: 12% and 8% in the energy mean and standard deviation, respectively. Thus, the energy and the amplitude of its fluctuations are not strongly dependent on $\alpha$.

The time series of the model integrations show that the model is relatively insensitive to changes in the value of $\alpha$, apart from the aforementioned effect on the relative amplitudes of the wave components. Therefore, $\alpha^{-1}$ was fixed at 5.625 days for the purposes of further analysis. This value was chosen because it allowed for a roughly equal partition of energy, on average, between the long and the short waves, in both mountain and no-mountain cases.

Finally, the complete parameter set used for the rest of this study is as follows:

$$\begin{aligned} k &= 0.01 \text{ or } (11.25 \text{ days})^{-1}, \\ k' &= 0.0025 \text{ or } (45 \text{ days})^{-1}, \\ \lambda &= 0.009 \text{ or } (12.5 \text{ days})^{-1}, \\ \theta^*_1 &= 0.1, \quad \beta' = 0.2, \\ \alpha &= 0.02 \text{ or } (5.625 \text{ days})^{-1}, \\ \sigma_0 &= 0.1, \quad n = 1.3, \quad h_2 = 0.2. \end{aligned} \tag{14}$$

Henceforth, these parameter settings will be referred to as the "standard set". In addition, some runs were performed with $h_2 = 0.4$, which will be referred to as the "high-mountain" runs.

## 5. Time-mean model flow

Time series of some model components are shown in Fig. 3 for the run using the standard set of parameters. Fig. 4 shows the same component time series for a run without topography (i.e., $h_2 = 0$). It can be seen that, in both the "mountain" and "no-mountain" cases, both high- and low-frequency quasi-periodicities are evident in an otherwise irregular pattern. The fairly regular 8-day period of the $\Psi_2$ component in Fig. 4 (no-mountain case) is due to a Rossby wave propagating without much interaction with other components. Such regular behavior is partially suppressed in the mountain case (Fig. 3). On the other hand, the presence of topography induces very high-frequency oscillations in the mean flow

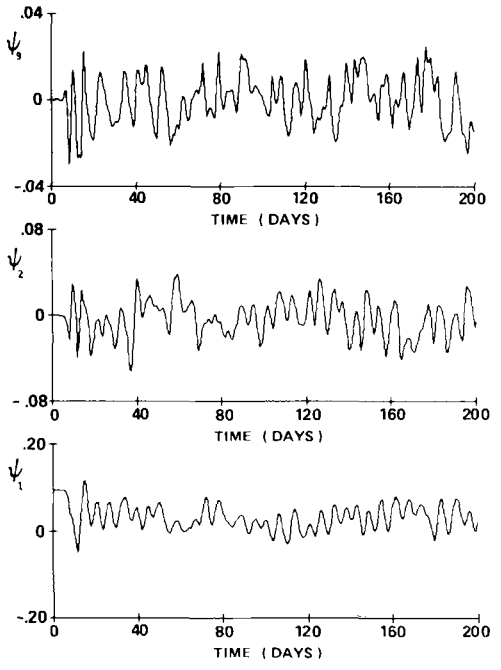


*Fig. 3.* Time series of barotropic streamfunction components $\Psi_0$, $\Psi_2$ and $\Psi_1$ for the standard set of parameters including topography ($h_2 = 0.2$). Extra damping at shortest scale has been included.

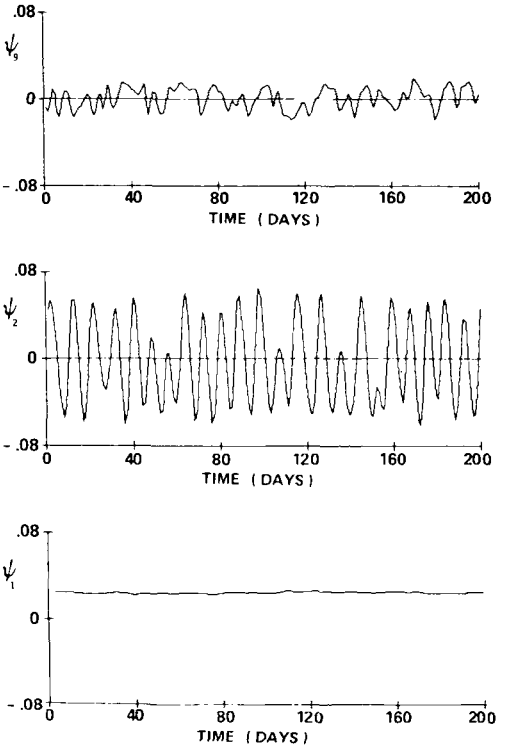


*Fig. 4.* As in Fig. 3 except for no-mountain case, i.e., $h_2 = 0.0$.

$\Psi_1$ and long-wave $\Psi_3$ components because of extra wave-mean flow interactions have been introduced by mountain-torque terms.

A more quantitative statistical summary is presented in Table 1, which lists the mean and standard deviation of each component for both the mountain and no-mountain cases over the last 1000 days of 1100-day runs. This table shows that eddy heat transports have reduced the time-mean temperature difference ($\theta_1$) acorss the channel from 0.095 (68°C) at Hadley equilibrium to 0.027 (21°C) in the mountain case and to 0.024 (18°C) in the no-mountain case. The presence of topography reduces the efficiency of the eddies in transporting heat, since it provides an asymmetric forcing which gives rise to a barotropic stationary wave. This forced wave tends to keep the temperature and wind fields in phase with each other. Relatively large mean magnitudes of $\Psi_2$ and $\theta_2$, in particular, account for the stationary wave in the mountain case. In the no-mountain case the eddy components all

Table 1. *Means and standard deviations of the 20 modal coefficients for the last 1000 days of a 1100 day run, for both the mountain and no-mountain cases*

| Component | Mean ($\times 10^3$) ($h_2 = 0.2$) | ($h_2 = 0.0$) | Standard deviation ($\times 10^3$) ($h_2 = 0.2$) | ($h_2 = 0.0$) |
|---|---|---|---|---|
| $\Psi_1$ | 29.3 | 24.3 | 24.0 | 1.0 |
| $\Psi_2$ | −3.2 | −2.0 | 17.0 | 33.1 |
| $\Psi_3$ | −0.7 | −0.8 | 19.3 | 32.7 |
| $\Psi_4$ | −1.8 | 1.0 | 19.8 | 27.4 |
| $\Psi_5$ | −0.5 | −0.2 | 15.6 | 19.2 |
| $\Psi_6$ | −0.6 | 0.8 | 16.7 | 18.9 |
| $\Psi_7$ | −0.0 | 0.7 | 16.6 | 14.6 |
| $\Psi_8$ | 0.8 | −0.2 | 17.0 | 14.5 |
| $\Psi_9$ | −0.0 | −0.5 | 10.8 | 8.9 |
| $\Psi_{10}$ | −0.1 | −1.6 | 10.7 | 8.5 |
| $\theta_1$ | 27.3 | 24.2 | 6.3 | 5.0 |
| $\theta_2$ | −13.2 | −1.2 | 7.1 | 9.7 |
| $\theta_3$ | −0.8 | −0.1 | 8.0 | 10.0 |
| $\theta_4$ | −0.3 | 0.2 | 6.5 | 8.2 |
| $\theta_5$ | −0.1 | 0.0 | 6.5 | 8.4 |
| $\theta_6$ | 0.4 | 0.2 | 6.9 | 7.9 |
| $\theta_7$ | −0.4 | 0.4 | 7.8 | 7.4 |
| $\theta_8$ | −0.3 | −0.1 | 7.9 | 7.3 |
| $\theta_9$ | −0.2 | −0.5 | 5.7 | 5.3 |
| $\theta_{10}$ | −0.1 | −0.8 | 5.7 | 5.1 |

have small mean values, which would tend to zero if the averaging period were increased to infinity.

In the mountain case, the total variance is spread fairly evenly among the different wave modes. In the no-mountain case the mode 22 compoments have relatively small standard deviations, while the mode 11 components have relatively large standard deviations. This is because the tendency towards a single-wave equilibrium was not very pronounced in the no-mountain case in the absence of extra damping on the shortest scale (i.e., $\alpha = 0$). The introduction of $\alpha$ further increases the ratio of long-wave to short-wave amplitude. The mean flow component $\Psi_1$ also has very small variability because the severe truncation and lack of topography prevents it from interacting with other scales.

Consistently less variance occurs in the thermal (baroclinic) components than in the streamfunction (barotropic) components, for both the mountain and no-mountain cases. It may be explained simply by noting that the baroclinic components are damped by Newtonian cooling as well as mechanical dissipation at the surface and interface. The barotropic components, on the other hand, are only affected by the mechanical dissipation.

Fig. 5 shows the time-mean and 300 mb (upper layer) geopotential height 500 mb (mid-level) temperature fields for the mountain case. The temperature field looks the same at all levels since $\sigma =$ constant. A stationary long wave is evident in all fields for the mountain case, although it is rather weak in the 500 mb height field. The zonal distance is measured in degrees relative to the topographic ridge which is centred at 0, +/− 360° along the zonal axis, so the stationary ridge in the height and temperature fields is situated just west of the valley. The mean lower-layer flow in the model consists of a closed cyclone over the valley and an anticyclone over the mountain ridge. This stationary wave flow does not correspond well to the observed flow over topography in the atmosphere. The model flow *over* the topography is too weak to generate more realistic time-mean stationary waves.

Maps similar to Fig. 5 for the no-mountain case are not shown, as there is little energy in standing waves in the time-mean circulation of

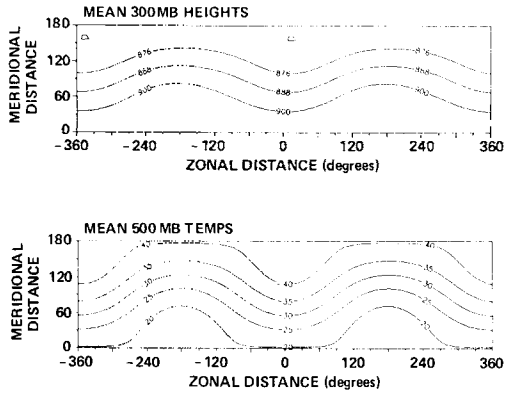


*Fig. 5.* Time-mean fields for standard set of parameters, including topography, for 300 mb heights and 500 mb temperatures. Axes are labelled in degrees, with $x$-axis labelled relative to topographic peak at $x = 0°$ and $\pm 360°$. Contour intervals are every 5°C for 500 mb temperatures and 120 m for 300 mb heights.

this case, and the standard deviations are also independent of longitude as expected. Standard deviation maps for the mountain case (Fig. 6) show a distinct "corridor" in the 500 mb heights along which eddy activity is concentrated. A similar asymmetry appears only weakly in the temperature standard deviations, although it is much more apparent in the mean and standard deviation fields from the "high mountain" runs.

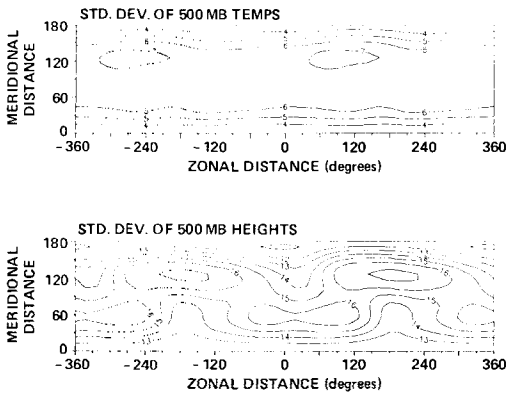


*Fig. 6.* Standard deviation fields for the standard parameter set for 500 mb temperatures and 500 mb heights. Contour intervals are every 1°C for 500 mb temperatures and 10 m for 500 mb heights.

## 6. Model variance

We next examine the types of variability and persistent anomalies which the model produces. Variance-conserving frequency spectra were obtained from Fourier transforms of the time series of each model component, along with coherence and phase plots for some related pairs of components. Let us consider the no-mountain case (Fig. 7) first as this is the simplest. Fig. 7a shows the frequency spectra for the $\Psi_2$ and $\Psi_3$ components. There is a single peak at about 8 days evident in both spectra with very little variance at other periods. The two components are highly coherent and almost exactly 90° out of phase at this frequency. This reflects the westward propagation of the large-scale Rossby wave which has little interaction with any of the other components of the flow. There are no low-frequency modulations of this wave at all.

In Fig. 7b for the mode 22 components, eastward-propagating Rossby waves are represented by the coherent narrow peaks at periods less than 8 days. However, at this scale there is a greater spread of variance along the spectrum. Frequency spectra for the mean flow components $\Psi_1$ and $\Psi_4$ are shown in Fig. 7c. The $\Psi_1$ variance is spread much more widely than in the wave components and is concentrated in the low-frequency range. While the total variance of $\Psi_1$ is very small, it is almost perfectly coherent at all frequencies with $\theta_1$, which has a larger total variance.

Frequency spectra for the mode 12 and mode 21 waves (not shown) present patterns intermediate to the mode 11 and mode 22 waves. In general, long zonal waves propagate slowly westwards and short waves propagate quickly eastwards, as revealed by peaks in their variance along with the high coherence and fixed phase between their components at certain frequencies. However, these intermediate components also have a broad spread of variance across the spectrum with many secondary, incoherent peaks which represent natural interaction frequencies with other components, barotropic or baroclinic.

To find out which components exchanged energy with the mean flow at each of the peaks in the $\Psi_1$ spectrum, plots of the coherence between the $\Psi_1$ time series and every other component time series were obtained. Except for the

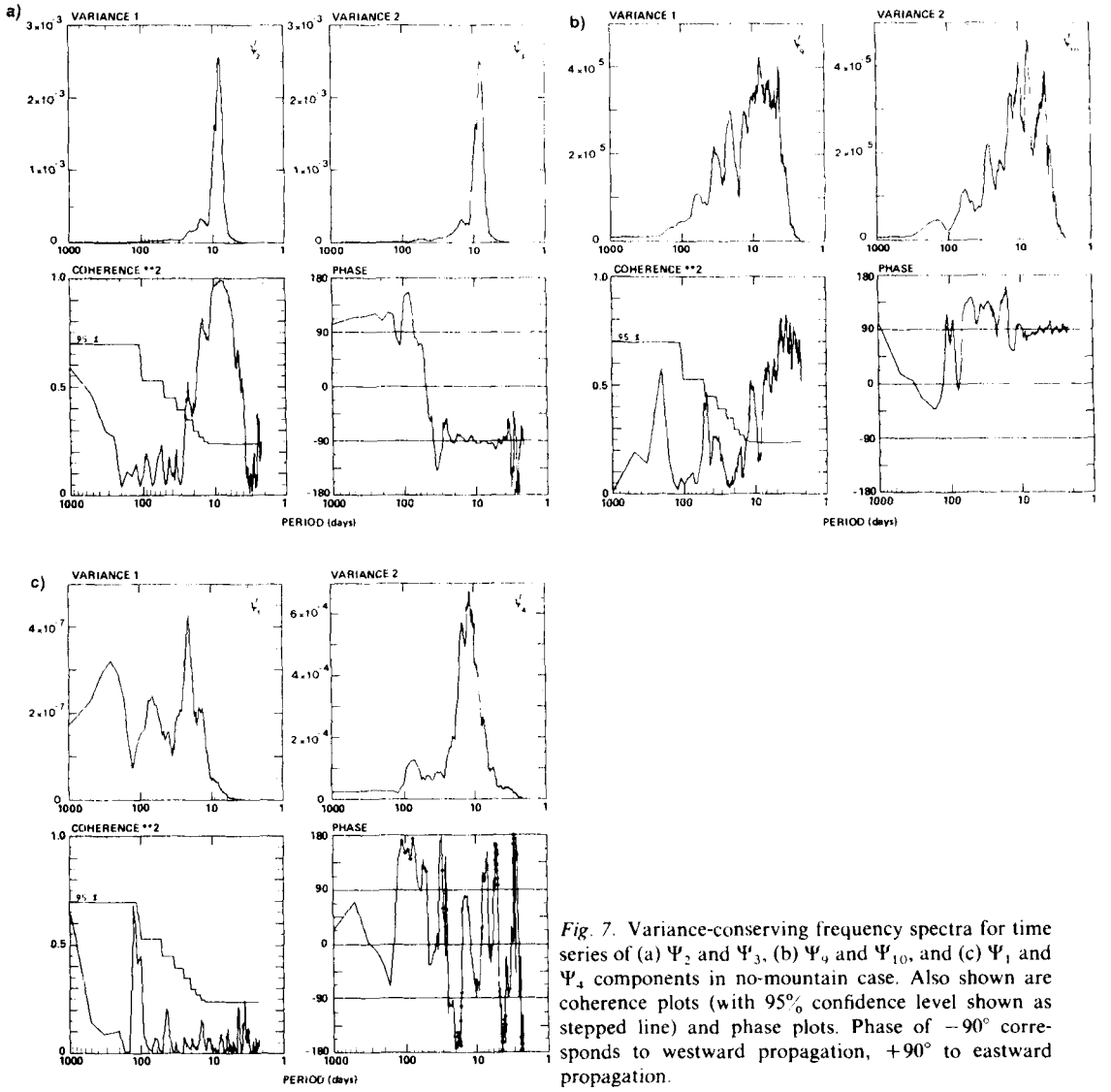


*Fig. 7.* Variance-conserving frequency spectra for time series of (a) $\Psi_2$ and $\Psi_3$, (b) $\Psi_9$ and $\Psi_{10}$, and (c) $\Psi_1$ and $\Psi_4$ components in no-mountain case. Also shown are coherence plots (with 95% confidence level shown as stepped line) and phase plots. Phase of $-90°$ corresponds to westward propagation, $+90°$ to eastward propagation.

comparison with $\theta_1$, the coherence rarely attained the 95% confidence limit for significance. Testing the $\Psi_4$ mean flow component for coherence with each of the other components likewise revealed little significant coherence except with $\theta_4$. It would seem from these results that constant-amplitude wave propagation dominates at all scales in the model and that little organized variability exists among the nonlinear interactions.

Frequency spectra for the mountain case with $h_2 = 0.2$ look very similar to those for the no-mountain case. The lower-layer flow is so weak in all the runs of this model that only a very high mountain can have a strong impact on the nature of the flow. The lower-layer flow is weak because the meridional truncation prevents a momentum flux convergence into the gravest meridional mode of the mean flow. In the atmosphere, this convergence maintains the surface flow against dissipation by surface friction and mountain torque. If the lower-layer winds were stronger, no doubt the lower mountain would have a stronger influence than is the case in this model.

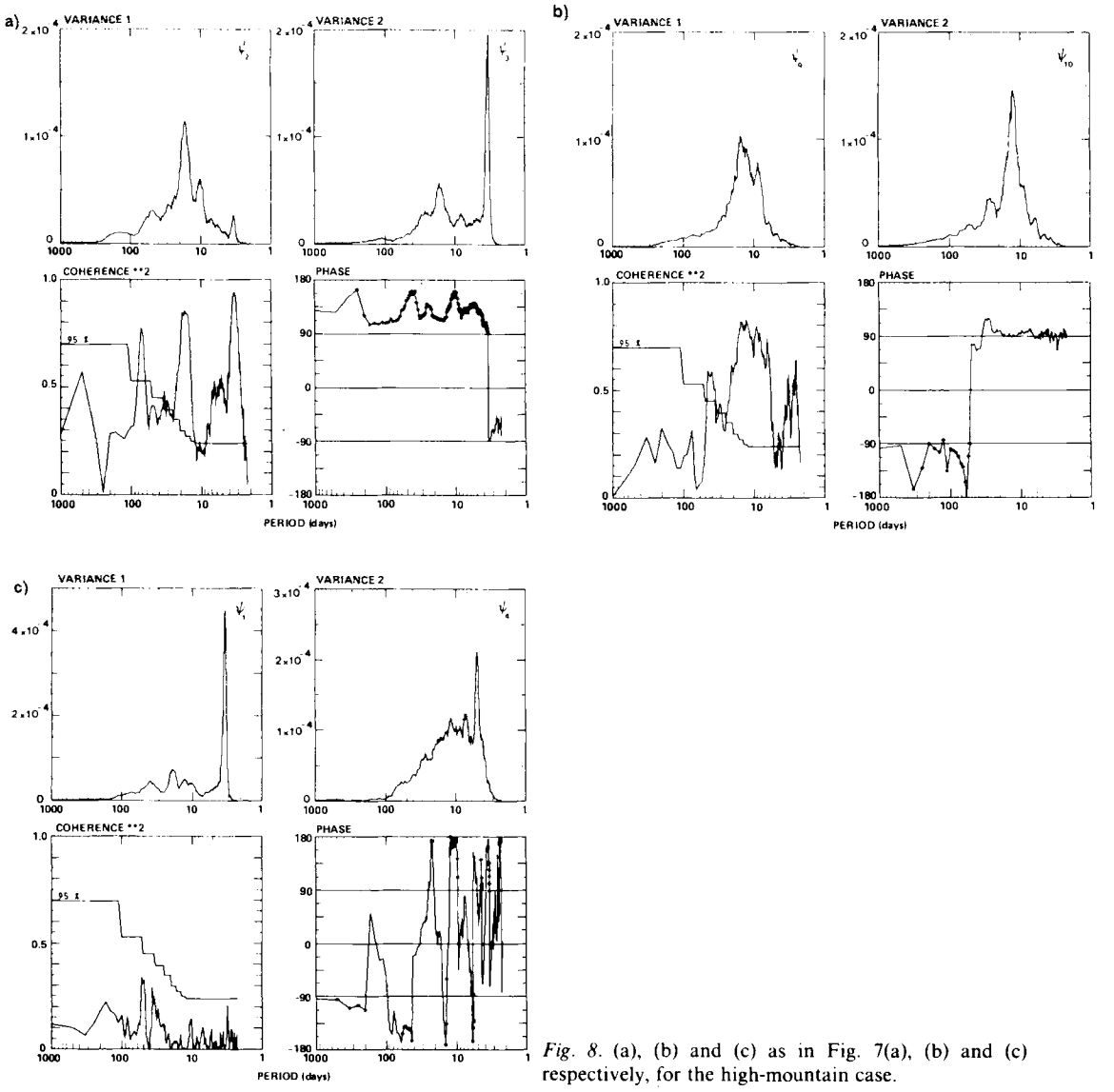


*Fig. 8.* (a), (b) and (c) as in Fig. 7(a), (b) and (c) respectively, for the high-mountain case.

Only for the "high mountain" run ($h_2 = 0.4$) do the frequency spectra look significantly different from the no-mountain case. Some spectra from this run are shown in Fig. 8. The nonlinear mountain torque terms in (6) give rise to the high frequency peaks at 3.5 days in the $\Psi_1$ and $\Psi_3$ spectra (Figs. 8c and 8a) and at 5 days in the $\Psi_4$ (Fig. 8c) and $\Psi_6$ spectra (not shown). Secondly, the propagating Rossby wave component is not so clearly dominant in the long waves (Fig. 8a) as it is in the short waves (Fig. 8b) or in the no-mountain case (Fig. 7a), since the mountain inhibits the propagation of these waves and gives rise instead to a stationary long wave. Even though the components are coherent at lower frequencies, they do not exhibit the fixed phase relationship of a propagating wave. The long (mode 11) wave components have a very broad spread of variance along their spectra relative to the no-mountain case.

A wealth of different wave-mean flow and wave-wave interactions are evident from the spectra of the mode 21 and mode 12 components (not shown), which have a significant amount of

energy at low frequencies which are not coherent with the other (barotropic) component of the same wave. The spectra for the components of the short mode 22 wave (Fig. 8b), however, show a lot of coherence between the two components and the prevalence of non-interacting, eastward-propagating waves with periods of less than 20 days. This rather slow propagation may be due to the weakness of the mean winds. The spectra of the mean flow components $\Psi_1$ and $\Psi_4$ are shown in Fig. 8c. The major spikes are due to the mountain torque interactions mentioned above. Otherwise, the $\Psi_1$ spectrum shows a fairly even spread of variance at periods up to 100 days or so. Variance at the shorter meridional scale ($\Psi_4$) is concentrated at shorter periods by comparison. Similar plots for the baroclinic or thermal components and other quantities show much the same kind of features and are not shown here.

## 7. Persistent anomalies

Anomalous states of the circulation may be quite steady and long-lived, although their presence may not show up as a peak in the frequency spectrum. Instead, they will contribute to a large spread in the background variance in the same way that a Fourier analysis of a square wave requires infinitely many harmonics to make the fit. Such persistent anomalies resemble stable flow configurations rather than slowly oscillating waves. In fact, they may be the dominant features of the flow, as in the "demonstration case" of the RP model which remains in one or another flow regime most of the time.

The present model was investigated for the occurrence of persistent anomalies. In order to facilitate better comparison with the atmosphere and the results of Dole and Gordon (1983), the model components were summed to produce time series of geopotential height and temperature fields, which were then tested for persistent anomalies at different gridpoints. Table 2 shows some of the results for the 500 mb height field of the high-mountain case. Persistent anomalies occurred in the no-mountain and low-mountain cases also, but were much fewer and shorter lived. All the gridpoints presented in Table 2 are at $y' = \pi/2$, i.e. the meridional mid-point of the channel. The corresponding longitudinal coordinates are chosen at the topographic peak ($x' = 0$), the topographic "valley" ($x' = \pi$) and at points on the downslope and upslope ($x' = \pi/2$, $x' = 3\pi/2$, respectively). It is apparent from Table 2 that there are two regions in the model where persistent anomalies are most likely to occur, near the points $(0, \pi/2)$ and $(\pi,\pi/2)$. In between these regions (i.e., around $(\pi/2, \pi/2)$ and $(3\pi/2, \pi/2)$) the occurrence of persistent anomalies is suppressed. The point $(0, \pi/2)$ reports the most long-lived positive events of any of the points shown in Table 2.

Furthermore, positive anomalies tend to occur preferentially over negative ones, especially for strong threshold criteria, although it is not easily seen in Table 2. Fig. 9 plots the number of positive and negative events which occur as a function of the duration threshold, for given magnitude criteria, at $(0, \pi/2)$. For weak thresholds, Table 2 shows that positive anomalies are predominant at $(0, \pi/2)$. However, Fig. 9

Table 2. *Persistent anomaly statistics of the 500 mb geopotential height field for various gridpoints and threshold criteria, based on 1000 model days; high-mountain case only*

| Threshold Magnitude | Duration (days) | | Gridpoint $(0, \pi/2)$ Pos | Neg | Tot | $(\pi/2, \pi/2)$ Pos | Neg | Tot | $(\pi, \pi/2)$ Pos | Neg | Tot | $(3\pi/2, \pi/2)$ Pos | Neg | Tot |
|---|---|---|---|---|---|---|---|---|---|---|---|---|---|---|
| 50 m | – | | 362 | 340 | 702 | 318 | 321 | 639 | 339 | 365 | 704 | 313 | 313 | 626 |
| 50 m | 7 | Days: | 141 | 131 | 272 | 23 | 38 | 61 | 143 | 146 | 289 | 23 | 45 | 68 |
| | | Events: | 15 | 15 | 30 | 3 | 4 | 7 | 14 | 16 | 30 | 2 | 6 | 8 |
| 50 m | 10 | Days: | 70 | 43 | 113 | 0 | 12 | 12 | 80 | 77 | 157 | 14 | 0 | 14 |
| | | Events: | 6 | 4 | 10 | 0 | 1 | 1 | 6 | 7 | 13 | 1 | 0 | 1 |
| 100 m | – | | 217 | 214 | 431 | 178 | 170 | 348 | 221 | 203 | 424 | 157 | 170 | 327 |
| 100 m | 7 | Days: | 75 | 45 | 120 | 7 | 7 | 14 | 38 | 29 | 67 | 0 | 0 | 0 |
| | | Events: | 9 | 6 | 15 | 1 | 1 | 2 | 5 | 4 | 9 | 0 | 0 | 0 |

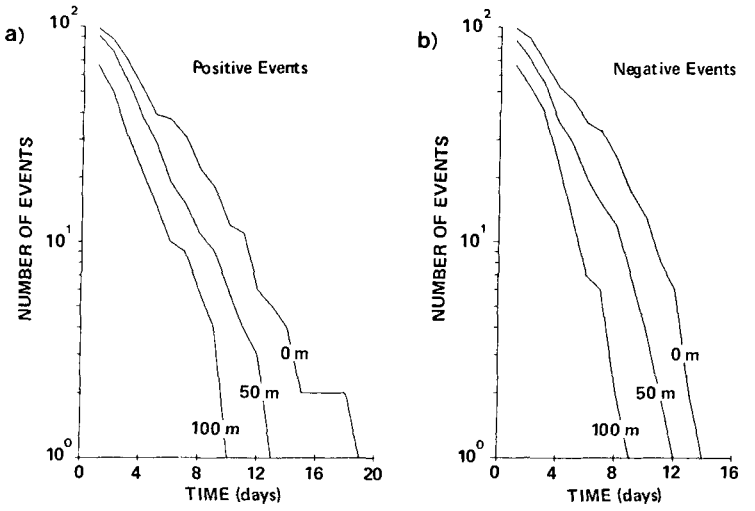


*Fig. 9.* Plots of the number of persistent anomalies which occur at point $(0, \pi/2)$, as a function of duration threshold. Top curve is for a magnitude threshold of 0 m, middle curve for a magnitude threshold of 50 m and lowest curve for a magnitude threshold of 100 m: (a) positive events; (b) negative events.

shows that positive events are distinctly preferred over negative ones for longer duration thresholds. This is true for all magnitude criteria chosen (0 m, 50 m, or 100 m).

An example of the persistence of a positive anomaly at the point $(0, \pi/2)$, where its recurrence is preferred, is shown in Fig. 10. This anomaly satisfies the 100 m, 10 day threshold criteria at the 500 mb level for the 11 days from day 511 through day 521; the 6 days shown are representative of the entire anomaly. A long wave ridge is evident over the topographic ridge throughout the anomaly period. Some of the energy conversion terms change sign during these 6 days, since the ridge orientation changes from southwest-northeast to northwest-southeast and back again during this period. The centre of the high also shifts from east of the topographic ridge to west and north of it. Since the sign of the mountain torque depends on whether the higher pressure is upstream or downstream of the mountain peak, the energy conversions due to mountain torque change sign as well.

The large amount of variation within the anomaly period is an indication that the anomaly itself is not a predetermined, artificially induced result but a genuine occasional product of the nonlinear dynamics of the flow. To date, simple model studies of persistent anomalies and blocking have tended to engineer the desired result by forcing it too directly. If a blocking flow was produced, it usually meant that the model could do nothing else but produce the block. For example, Tung and Lindzen (1979) and Mitchell and Derome (1983) produced plausible-looking blocks based on the resonance of Rossby waves with underlying topography. However, they depended on either linearity or some other non-interaction condition in order to prevent the flow from moving off resonance.

Persistent anomaly statistics for the thermal components (not shown) reveal that the persistent height anomalies coincide with anomalies in the temperature field of the same sign. Since the height field of the upper model level (about 300 mb) is proportional to $\Psi + \theta$ and the height field of the lower level (850 mb) is proportional to $\Psi - \theta$, this means that the persistent anomalies have an equivalent barotropic structure, with the anomalies stronger at the upper level and weaker at the lower level.

## 8. Conclusions

We have investigated the properties of a two-level low-order model which incorporates wave-

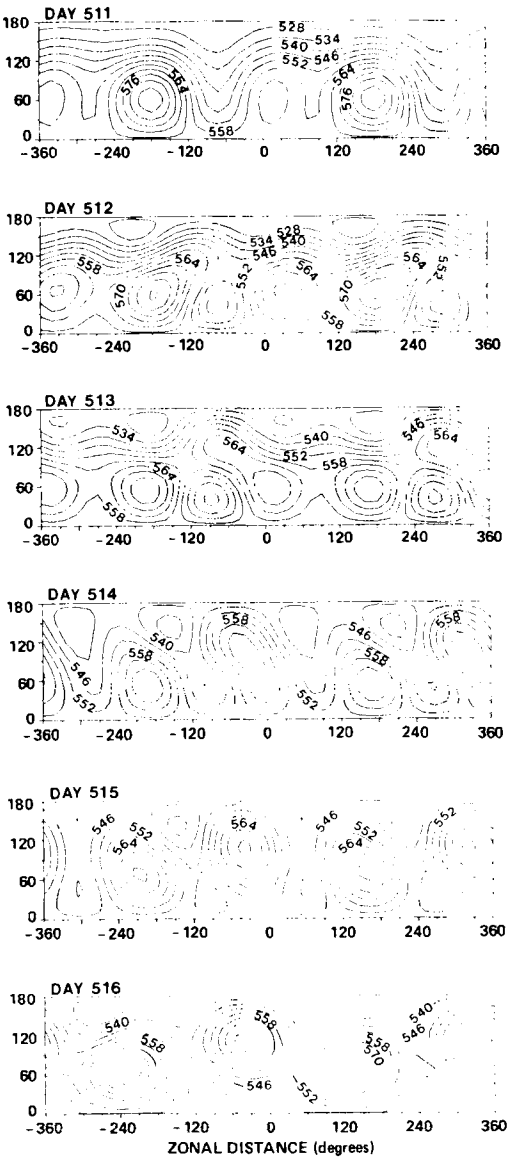


*Fig. 10.* 500 mb height fields for 6 days (day 511-516) during a persistent anomaly which satisfied threshold criteria of (100 m, 10 days) at point (0, $\pi/2$) between days 511 and 521. Axes are labelled as in Fig. 5. The contour interval is 60 m.

wave as well as wave-mean flow interactions. A similar model was described in RP but had unrealistic thermal and dissipative time scales. We varied these time scales, and then fixed them at more "earth-like" values. Since these changes alone did not produce an earth-like flow because of a spurious energy build-up in the smallest scale, we included extra damping at this scale to parametrize the effects of smaller unresolved waves. When integrated for 1100 days, the model then produced a more realistic-looking flow without exhibiting the dominant regime-type behavior of the RP model.

The differences between the mountain and no-mountain model cases have been examined at each step of this study. The higher mountain gave rise to a standing long wave in the time-mean flow and tended to "phase lock" the long Rossby waves. It also caused variance peaks to appear in the large scale flow at low frequencies (Fig. 8a) which did not exist in the no-mountain case (Fig. 7a) and appeared only weakly in the low-mountain case. However, a rich variety of amplitude modulations and other low-frequency oscillations were present in both the mountain and no-mountain cases.

Persistent anomalies in the behavior of the large-scale wave were not nearly as large or as long-lasting as the regimes obtained by RP. Persistent anomalies in the 500 mb height field were found to occur preferentially in the region around the topographic ridge. More positive than negative events occurred there for all the threshold criteria chosen. Anomalies in the thermal field were in phase with the persistent anomalies in the 500 mb heights so that the anomalies had an equivalent barotropic structure.

The realism and validity of the model is restricted by the fact that the zonally averaged momentum balance is unrealistic, due to the severe truncation which prevents the convergence of momentum flux into the gravest meridional mode of the mean flow; a feature which is common to many low-order models incorporating baroclinic waves. This convergence normally acts to maintain the westerlies by counteracting the effects of mountain torque and surface friction. Its absence leads to weaker-than-observed westerlies and also to the unrealistic positioning of the mean ridge in the height fields relative to the topographic ridge. The inclusion of an extra meridional and zonal wave and some other minor refinements would remove at least some of these shortcomings. The model, as it stands, also excludes certain interactions among waves not directly forced by topography, which

normally provide a path for enstrophy cascade to the short scales as in the converged high-resolution model of CT. The presence of the extra dissipation at the shortest scale compensates somewhat for this deficiency.

While this model does not produce multiple equilibria or multiple weather regimes, it does produce multiple anomalous states in the context of a highly variable circulation. This suggests that the basic physical mechanisms discussed by Charney and Straus and RP only sporadically come into play when forcing and damping time scales are made more realistic and compensation is made for the cascade effects of unresolved scales.

## 9. Acknowledgements

We would like to express our gratitude to Liz Williams for providing many of the time-series analysis programs used in this study, to Don Olson for giving us access to the MACSYMA mathematical package and to two anonymous reviewers for helpful suggestions. The first author acknowledges the support of a University of Miami fellowship during the early part of this work and both authors acknowledge the support of the Global Scale Atmospheric Processes Research Program of NASA Headquarters under Grant NAG8-656, administered by Marshall Space Flight Center.

## REFERENCES

Barnes, J. P. 1986. Finite amplitude behavior of a single baroclinic wave with multiple vertical modes: effects of thermal damping. *J. Atmos. Sci. 43*, 58–71.

Blackmon, M. L., Mullen, S. L. and Bates, G. T. 1986. The climatology of blocking events in a perpetual January simulation of a spectral general circulation model. *J. Atmos. Sci. 43*, 1379–1405.

Cai, M. and Mak, M. 1987. On the multiplicity of equilibria of baroclinic waves. *Tellus 39A*, 116–137.

Cehelsky, P. and Tung, K. K. 1987. Theories of multiple equilibria and weather regimes—a critical reexamination. Part II: baroclinic two-layer models. *J. Atmos. Sci. 44*, 3282–3303.

Charney, J. G. and deVore, J. G. 1979. Multiple flow equilibria in the atmosphere and blocking. *J. Atmos. Sci. 36*, 1205–1216.

Charney, J. G. and Straus, D. M. 1980. Form-drag instability, multiple equilibria, and propagating planetary waves in baroclinic, orographically forced, planetary wave systems. *J. Atmos. Sci. 37*, 1157–1176.

Dole, R. M. 1986. Persistent anomalies of the extratropical northern hemisphere wintertime circulation. *Mon. Wea. Rev. 114*, 178–207.

Dole, R. M. and Gordon, N. D. 1983. Persistent anomalies of the extra-tropical Northern Hemisphere wintertime circulation. Geographical distribution and regional persistence patterns. *Mon. Wea. Rev. 111*, 1567–1586.

Egger, J. 1978. Dynamics of blocking highs. *J. Atmos. Sci. 35*, 1788–1801.

Hendon, H. H. 1986. Time-mean flow and variability in a nonlinear model of the atmosphere with orographic forcing. *J. Atmos. Sci. 43*, 433–448.

Källén, E. 1981. The nonlinear effects of orographic and momentum forcing in a low-order, barotropic model. *J. Atmos. Sci. 38*, 2150–2163.

Källén, E. 1982. Bifurcation properties of quasi-geostrophic, barotropic models and their relation to atmospheric blocking. *Tellus 34*, 255–265.

Legras, B. and Ghil, M. 1985. Persistent anomalies, blocking and variations in atmospheric predictability. *J. Atmos. Sci. 42*, 433–471.

Lorenz, E. N. 1971. N-Cycle time differencing for stepwise numerical integration. *Mon. Wea. Rev. 99*, 644–648.

Mak, M. 1985. Equilibration in nonlinear baroclinic instability. *J. Atmos. Sci. 42*, 2764–2782.

Mitchell, H. L. and Derome, J. 1983. Blocking-like solutions of the potential vorticity equation: their stability at equilibrium and growth at resonance. *J. Atmos. Sci. 40*, 2522–2536.

Mukougawa, H. 1987. Instability of topographically forced Rossby waves two-layer model. *J. Met. Soc. Japan 65*, 13–24.

Pedlosky, J. 1970. Finite amplitude baroclinic waves. *J. Atmos. Sci. 27*, 15–30.

Reinhold, B. B. and Pierrehumbert, R. T. 1982. Dynamics of weather regimes: quasi-stationary waves and blocking. *Mon. Wea. Rev. 110*, 1105–1145.

Reinhold, B. B. and Pierrehumbert, R. T. 1985. Corrections to "Dynamics of weather regimes: quasi-stationary waves and blocking". *Mon. Wea. Rev. 113*, 2055–2056.

Salmon, R. 1980. Baroclinic instability and geostrophic turbulence. *Geophys. Astrophys. Fluid. Dyn. 15*, 167–211.

Shukla, J. and Mo, K. C. 1983. Seasonal and geographical variation of blocking. *Mon. Wea. Rev. 111*, 388–402.

Tung, K.-K. and Lindzen, R. S. 1979. A theory of stationary long waves. I. A simple theory of blocking. *Mon. Wea. Rev. 107*, 714–734.

Tung, K.-K. and Rosenthal, A. J. 1985. Theories of multiple equilibria—a critical reexamination. Part I: Barotropic models. *J. Atmos. Sci. 42*, 2804–2819.

Yoden, S. 1983. Nonlinear interactions in a two-layer, quasi-geostrophic, low-order model with topography. Part II: Interactions between zonal flow, forced waves and free waves. *J. Meteor. Soc. Japan 61*, 19–35.